Applied Surface Science Advances 27 (2025) 100726

Contents lists available at ScienceDirect

Applied Surface Science Advances

journal homepage: www.sciencedirect.com/journal/applied-surface-science-advances

Full Length Article

# The effect of copper additives on hybrid Zr-based chemical conversion coating morphology and chemical compositions

Ankita Mohanty [a], Xiaoyang Liu [a], Cheng-Chu Chung [a], Donald Vonk [b], Kim Kisslinger [c], Xiao Tong [c], Andrew Kiss [e], Gary Halada [a], Stanislas Petrash [d], Kate Foster [b], Yu-chen Karen Chen-Wiegart [a,e,*]

[a] Department of Materials Science and Chemical Engineering, Stony Brook University, Stony Brook, NY 11794, USA
[b] Henkel Corporation, Madison Heights, Michigan 48071, USA
[c] Center for Functional Nanomaterials, Brookhaven National Laboratory, Upton, New York 11973, USA
[d] Henkel Corporation, Bridgewater, New Jersey, 08807, USA
[e] National Synchrotron Light Source II, Brookhaven National Laboratory, Upton, New York 11973, USA

ARTICLE INFO

*Keywords:*
Conversion coating
Surface treatment
XANES
XRF

ABSTRACT

In the realm of corrosion protection, Zr-based conversion coatings offer an environmentally friendly, chromate-free alternative to conventional coating. This study uses advanced X-ray, electron microscopy and electrochemical testing techniques to better understand the impact of varying $Cu^{2+}$ ion concentrations on the characteristics of Zr-based coatings on Fe substrates. Our findings demonstrate that within the tested conditions, higher $Cu^{2+}$ additive concentrations at 40 ppm enhance surface characteristics, increasing stability towards anti-corrosion capability, particularly under NaCl treatment. Conversely, at a lower $Cu^{2+}$ concentration of 20 ppm, coatings exhibited more significant dissolution of Cu clusters and increased vulnerability to chloride-induced degradation. X-ray photoelectron spectroscopy and synchrotron X-ray fluorescence (XRF) and X-ray absorption near edge structure (XANES) spectroscopy analyses revealed $Cu^{2+}$ formation in Cu20, while Cu40 retained its metallic state ($Cu^0$) with a slower reaction rate. Cu20 offers some protection but lacks durability, whereas in Cu40, lower $I_{corr}$, and enhance corrosion resistance, making it ideal for protective coatings in salt-water environments. This study underscores the importance of balancing $Cu^{2+}$ ions concentration in the coating solution to optimize performance, highlighting the role of Cu in enhancing both surface properties and long-term stability.

## 1. Introduction

Our civilization is routinely impacted by corrosion, which degrades and damages many objects, including automobiles, aircraft, bridges, and other infrastructure. Based on data from the U.S. Census as of July 1, 2001, the current per capita direct cost of corrosion for citizens of the U. S. is around $970 per person per year [1]. Steels, Zn-coated (galvanized) steels, and Al alloys are the primary metals used in the U.S. to produce goods and facilities in most applications, including industrial infrastructure [2]. However, corrosion of these metallic parts is of paramount concern. Researchers have developed various methods to prevent corrosion, including the application of polymer liners, implementation of cathodic protection, and use of corrosion inhibitors [3]. Chemical conversion coatings are recognized as a highly cost-effective technique for modifying surfaces [4]. Conventional hexavalent chromium (Cr-VI), zinc phosphate ($Zn_3(PO_4)_2$), and trivalent chromium $(Cr\text{-}III)_5$ are already available. However, these chromate coatings are highly toxic and carcinogenic, raising environmental and public health concerns. Similarly, phosphate ($PO_4^{3-}$) coatings are responsible for eutrophication in freshwater [5]. Consequently, researchers have sought to develop new eco-friendly conversion coatings that can be applied at ambient temperature while still providing satisfactory protection and cost savings.

Previous studies have explored eco-friendly coatings and nanocomposites with rare-earth elements like Li and Zr, though few have shown commercial potential. Recent research focuses on Zr-based chemical conversion coatings, along with elements like Ce, combined with $Zn_3(PO_4)_2$ post-treatment, showing improved corrosion resistance performance. However, the process remains time-intensive and is not ready for widespread industrial use [6,7]. Notably, coatings based on Zr

* Corresponding author.
*E-mail address:* Karen.Chen-Wiegart@stonybrook.edu (Y.-c.K. Chen-Wiegart).

https://doi.org/10.1016/j.apsadv.2025.100726
Received 20 December 2024; Received in revised form 20 February 2025; Accepted 4 March 2025
Available online 26 March 2025

have emerged as a superior alternative to traditional options. These Zr-based coatings are gaining traction in various fields, offering the possibility of reducing costs related to energy, maintenance, and environmental impact. This Zr-based conversion coating is an exciting alternative as it can provide excellent corrosion protection at a reasonable price and was first introduced to the automobile industry in 2005 [8]. These coatings are created by submerging a substrate in a chemical bath, reacting with the metal substrate to coat the surface with a protective layer [9]. The main goal is to increase the adherence to the following paint coats that are applied [10]. Hexafluorometallate complexes (such as $H_2ZrF_6$, $Na_2ZrF_6$, and $H_2TiF_6$) inorganic acids are commonly found in conversion baths, along with additives that control the mechanism of film formation or adhesion qualities. Hexafluorozirconic acid ($H_2ZrF_6$) has been successfully applied on substrates such as Al alloy, Mg alloy, Zn, and Zn-coated alloys and steels [11–14]. However, hexafluoride carries the impression of giving rise to highly smooth coating surfaces which have a deteriorating impact on the cohesion effect of paints [15]. Other surface modification techniques can give rise to several tangled crystals at the metal top layer, enhancing the paint bonding strength due to better-interlocking capacity [16,17]. Therefore, combining organic and inorganic additives could be beneficial in enhancing the adhesion of the subsequent paint layer applications.

Previous research [18,19], has investigated the formation of coatings and the influence of various inorganic additives, such as Cu, V, and Ce ions, on different metal substrates. In particular, studies have focused on the effects of adding $Cu^{2+}$ to Zr-based conversion coatings. For example, *Liu* et al. explored the role of Polyamidoamine (PAMAM) and Cu additives in hybrid Zr-based chemical conversion coatings. They identified an optimal PAMAM concentration of 50 ppm to prevent void formation and enhance coating adherence. Increasing PAMAM concentrations reduced the number of Cu clusters without significantly changing their diameter [19]. Similarly, *Adhikari* et al. observed that when TecTalis® coatings were applied to steel, the inclusion of Cu provided better resistance to delamination, emphasizing the potential of Cu to enhance the overall performance of Zr-based coatings [5].

Adding cupric ions as inorganic additives can facilitate Cu deposits on the metal surface [20]. These deposits act as extra cathodic sites for the reduction process during conversion, accelerating the rise in pH and boosting the deposition of Zr-hydroxides [20,21]. When used in appropriate amounts, Cu offers several advantages. For instance, Cu can enhance the corrosion protection of the coating. In combination with Zr, Cu forms a passive oxide layer that can protect the underlying metal substrate from environmental factors, making the coating more resilient. Additionally, when Cu ions are uniformly distributed, they can create a vital interface between the substrate and the top layer, improving paint adhesion and resulting in longer-lasting coatings. However, Cu plays a dual role in Zr-based conversion coatings, acting as both a beneficial and a detrimental additive depending on its concentration and deposition control. Excess Cu in the coating can cause significant problems. It can lead to large clusters or agglomerates forming on the surface, increasing surface roughness and non-uniformity. This can impair paint strength, leading to issues such as peeling or flaking over time. Furthermore, large Cu clusters reduce the overall durability of the coating, as non-uniform Cu distribution can create weak points in the coating structure. These weak points can make the coating more susceptible to damage, shortening its lifespan. Another critical issue with excess Cu is its ability to induce galvanic corrosion [22]. Cu is more electrochemically noble than many metals, meaning it is less likely to corrode itself but can accelerate the corrosion of metals like Fe or steel when in contact with an electrolyte (*e.g.*, water). In surroundings with moisture or electrolytes, excess Cu can cause rapid degradation of the metal substrate. Therefore, developing Zr-based coating baths that carefully control Cu levels is essential for optimizing coating performance and longevity.

In addition, these hybrid coatings can be applied on automobile bodies as a surface pretreatment to prevent degradation as the thick, Zr-rich oxide layer acts as a dense barrier, inhibiting electron transfer at the interface [23]. However, during winter, the most challenging season, the weather conditions can significantly affect coating conditions and automobile bodies. To manage winter road maintenance and reduce pavement slipperiness, chemical materials based on chlorides, such as NaCl, $CaCl_2$, and their mixtures, are utilized in significant yearly quantities on roads and streets. These chloride-based salts can lead to the corrosion of automobiles, roads, and reinforced concrete structures and the deterioration and deformation of road pavements [24].

In particular, previous research has focused on Zr-based conversion coatings with $Cu^{2+}$ additives, which showcased how $Cu^{2+}$ enhances corrosion protection on cold-rolled steel substrates [25]. Studies have mostly pinpointed the effect of the amount of organic additives in the solution, its formation mechanism, and its enhancements to improve coating performance characteristics [26]. This current study delves into the underexplored effects of varying $Cu^{2+}$ ion concentrations in coating solutions on the morphology of the coating film and chemical composition change within the substrate. The aim is to understand how different $Cu^{2+}$ amounts influence the coating, focusing on unraveling the coating formation mechanism. Additionally, considering the detrimental effects of winter conditions, particularly the use of NaCl-based deicers on coating longevity and vehicle durability, our research evaluates coating performance in NaCl environments. The coating samples were subjected to 3.5wt% NaCl solutions, simulating the application of road salt during harsh winter conditions. For a detailed analysis, the coatings were examined using a combination of electron microscopy and X-ray techniques. This multimodal approach allowed us to understand the variances in the Cu−PAMAM coatings and the reaction of the coating with NaCl. Scanning electron microscopy (SEM), focused ion beam (FIB)-SEM, and high-resolution scanning transmission electron microscopy (STEM) were utilized to understand the Cu cluster distribution and its size within the coating film. X-ray photoelectron microscopy (XPS) with Ar sputtering depth profiling was used to observe variations in elemental ratios and chemical composition within the coating. Moreover, the chemical composition of coatings produced under various conditions was investigated using X-ray absorption near edge structure (XANES), and this analysis was further supported by *in situ* synchrotron X-ray fluorescence (XRF) microscopy, where the changes in the X-ray fluorescence signals of chemical elements during the coating deposition was examined. This research enhances our understanding of the development of hybrid coating and performance in salt, which is informed by varying inorganic additive concentrations. These findings are instrumental in designing advanced surface coatings tailored to resist winter conditions more effectively.

## 2. Methods and characterization

### 2.1. Preparation of thin-film and cold-roll steel substrate

The low-carbon steel (LCS) sheets (1008 CRS) were purchased from ACT Test Panels. The CRS substrates were cut into 10 × 10 $mm^2$ and polished with SiC papers. Before the coating process, the substrates were sonicated in isopropanol alcohol (IPA) for 10 min to clean the polishing residue and any impurities left on the surface. The cleaned substrates were then dried by compressed air.

The thin-film samples were prepared on cut Si wafer substrates (500 μm, UniversityWafer, Inc., USA) with 10 × 10 $mm^2$ in a square at the Center for Functional Nanomaterials (CFN) at Brookhaven National Laboratory (BNL). The Si wafer was first cleaned by oxygen plasma for 150 s (Plasmaetch PE-50, 100 watts, 200–350 mtorr). The Fe thin film was then deposited by electron beam evaporation using Kurt J.Kesker PVD 75. The 99.995 % high-purity of Fe evaporation material was adopted. The thin-film deposition process was conducted at a ~5 Å/s rate with a high voltage of 7.8 kV under a vacuum of 1 × $10^{-6}$ Torr to grow ~100 nm Fe thin film.

### 2.2. Chemical conversion coating solution preparation

The conversion coating solutions were created by combining various quantities of $Cu^{2+}$ (0, 5, 10, 20, and 40 ppm) with a constant quantity of PAMAM (50 ppm). The sample I.D. is defined as Cu00, Cu05, Cu10, Cu20, and Cu40, corresponding to the $Cu^{2+}$ concentration of the solution used to prepare the coating. The conversion coating solution is composed of hexafluorozirconic acid with Cu added as cupric nitrate, $Cu(NO_3)_2$, to keep a Zr content of 50–300 ppm and a PAMAM content of 50 ppm in solution. The pH of all liquids was set to 4.0. Information about the Zr-based conversion coating solutions has been documented in earlier publications [18].

### 2.3. Deposition of chemical conversion coating on the substrate

The pretreatment of the chemical conversion coating process was the substrate cleaning in an alkaline solution (pH ~ 11.7), Bonderite C-AK T51 (Henkel Corporation, Madison Heights, MI). The solution, containing potassium hydroxide (KOH), sodium hydroxide (NaOH), sodium nitrite ($NaNO_2$), and sodium silicate ($Na_2SiO_3$), was used to clean the substrate in a 150 ml glassy beaker for 120 s at 48 °C in a water bath and followed by rinsing in a DI water for 60 s. The as-treated substrates were then immersed into the hybrid coating solutions for 120 s at 32 °C for the growth of the coating film. The hybrid coating solution, Bonderite M-NT 1820 with $H_2ZrF_6$ with PAMAM and Cu compound additive, was supported by Henkel Corporation (Madison Heights, MI). Finally, the samples were rinsed in DI water for 60 s to wash away the solution residue and dried with compressed air at an ambient temperature. The coating formation method is shown in Fig. 1A.

### 2.4. Characterization of coating film on the surface-SEM, FIB-SEM STEM, and XPS

Scanning electron microscopy (JEOL 7600F SEM) operating at 5.0 keV accelerating voltage was conducted to characterize the surface morphology of the coating samples. The SEM images were segmented using in-house developed Python code to calculate the diameter and the density of the Cu clusters on the coated samples. A dual-beam scanning electron/focused ion beam microscope (FIB-SEM FEI Helios) was applied to perform and prepare the cross-sectional image and lift-out specimen of the coating samples for transmission electron microscopy (TEM) characterization, respectively. The Pt layer on the top of the surface coating was deposited as a sacrificial layer for the trimming process. After multiple steps of thinning the thickness by gallium ion ($Ga^+$) milling, the lift-out specimen was mounted to the omniprobe lift-out Mo grids (Ted Pella, Inc.). High-resolution analytical scanning/transmission electron microscope (S/TEM, FEI Talos F200X) equipped with high-angle annular dark-field (HAADF) and EDS analysis was performed to reflect the elemental distribution and the coating profile. The STEM/EDS analysis was also carried out for the Cu10 and Cu40 coated samples after immersing them in NaCl solution for 24 hrs, and they were compared with those before treatment with NaCl solution. The elemental distribution and chemical composition from the surface inward the inside of the coating was characterized by X-ray photoelectron spectroscopy (XPS) in an ultrahigh-vacuum (UHV) system $< 2 \times 10^{-9}$ torr equipped with a hemispherical electron energy analyzer (SPECS PHOIBOS 100) and twine anode X-ray source (SPECSM XR50) with Al Kα (1486.6 eV) radiation. Argon ion ($Ar^+$) sputtering with a 500-eV kinetic energy was conducted to mill the surface layer by layer with different sputtering times to observe the elemental atomic ratio and composition along the various depths. The XPS results, referring to the C 1 s peak at 284.8 eV with Shirley background subtraction, were calibrated and fitted using CasaXPS software. All instruments mentioned above were conducted at the Center of Functional Nanomaterials (CFN) at Brookhaven National Laboratory (BNL).

### 2.5. NaCl treatment and in situ synchrotron X-ray fluorescence microscopy (XRF)

*In situ,* synchrotron XRF and micro-X-ray absorption near edge structure spectroscopy (μ-XANES) focusing on the Zr, Cu, and Fe K-edge were conducted with the help of high-resolution X-ray spectroscopy. This work utilized the submicron resolution capabilities of the synchrotron radiation X-ray (SRX, 5-ID) beamline at the National Synchrotron Light Source II (NSLS-II) located at Brookhaven National Laboratory (BNL). The X-ray energy used in the experiment was adjusted

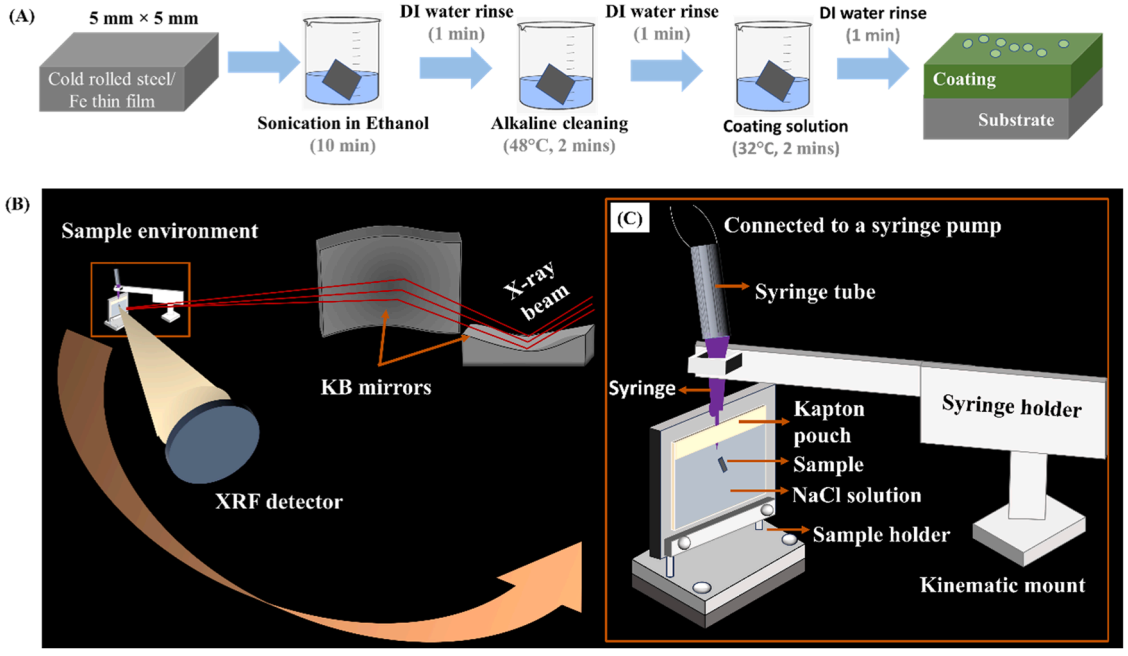


**Fig. 1.** Experimental setup (A) Preparation of Zr-based conversion coating on CRS and Fe thin film substrate, (B) Setup at SRX beamline, and (C) Schematic of the sample environment.

to 19.0 keV to detect fluorescence signals from the various elements- Cu, Fe, and Zr. For the investigation of a 3.5 wt.% NaCl *in situ* treatment, NaCl solution was methodically introduced into the sample, enclosed within a pouch cell composed of Kapton tape. The NaCl was injected using a Chemyx syringe pump, which was linked to the cell via an intricate tubing system. Fig. 1B shows the sample setup for the *in situ* synchrotron XRF experiment at the SRX beamline. Fig. 1C shows the schematic of the sample environment.

XRF elemental mapping was performed before the NaCl treatment to assess the elemental distribution in the Cu20 and Cu40 samples. The mapping covered 90 × 90 μm² areas at both the center and corners of the sample, with a precise step size of 0.25 μm. Additionally, smaller ROIs measuring 20 × 20 μm² were mapped for more detailed comparison and visualization within the larger regions.

The *in situ* experiment involved immersing the sample in a NaCl solution. XRF counts were systematically collected from alternating smaller regions, each sized at 5 × 2 μm², at the center and the solution region. This process aimed to quantify the intensity of various elements over time at different locations and was repeated 14 times. During the 15th scan, XRF maps from a larger central area of 15 × 15 μm² were collected to observe changes in morphology over time. The fluorescence counts for each element from this scan were also plotted to illustrate their variation. This continuous data collection and measurement cycle was conducted around the clock, completing 25 cycles on each sample. The resultant fluorescence counts were plotted as a function of time using Python codes developed in-house, thereby providing a dynamic profile of elemental variations and the reaction taking place during the treatment process.

Post-experiment, additional data was collected from the same locations where data had been collected before the *in situ* analysis, the large 90 × 90 μm² regions and the smaller ROIs measuring 20 × 20 μm² at both the center and corners of the sample, to enable comparison of morphology before and after treatment.

XANES data were also gathered for both pristine and *in situ* samples, before and after the solution injection, at both the corner and center of the samples. The standard samples for the energy calibration and reference, such as Cu foil, $CuF_2$, Cu $(OH)_2$, $CuCl_2$, CuO, $Cu_2O$, $ZrO_2$, and Fe, were measured in a transmission mode at the same beamline. The XANES of $Cu^{2+}$ ions in $CuCl_2$ solution were also measured at Beamline for Materials Measurement (BMM, 6-BM), National Synchrotron Light Source II (NSLS-II) located at Brookhaven National Laboratory (BNL) to confirm the final state of the Cu after the treatment.

### 2.6. Electrochemical test

The electrochemical behavior of the base metal and surface composites were studied to understand the corrosion resistance by conducting potentiodynamic polarization (PDP), using the GAMRY Reference 600+ instrument. A 3.5wt% NaCl solution was used as an electrolyte. All the testing were performed at room temperature (25 °C) and static electrolyte conditions. A three-electrode cell setup was used in a corrosion flask cell for the testing. The test samples were used as the working electrode (WE), a graphite rod was used as the counter electrode (CE), while the saturated calomel electrode acts as a reference electrode (RE). All the potentials were measured with respect to the potential of saturated calomel electrode (SCE), which is 0.242 V *vs* standard hydrogen electrode (SHE) potential. An open circuit potential (OCP) was measured for 25 hrs to condition the sample in the electrolytic environment. All the results were analyzed using EClab software.

The PDP test is considered destructive due to changes in surface chemistry during the experiment. A PDP curve is generated when the variation in current is monitored with respect to the change in the voltage applied to an electrochemical system. The plot has two parts: the cathodic and the anodic polarization curve. The Tafel approximation is used in the region where the anodic and cathodic polarization curves are linear. Tafel fit gives corrosion potential ($E_{corr}$) and corrosion current density ($I_{corr}$) The $E_{corr}$ is the neutral region where the anodic and cathodic reactions would be in equilibrium. The $I_{corr}$ value signifies the kinetic part of the reaction and provides the corrosion rate in a particular media.

## 3. Results and discussion

### 3.1. Effect of $Cu^{2+}$ ions on the morphology of the coating film

The characteristic surface of the pristine uncoated substrate and the coated CRS, with increasing concentrations of $Cu^{2+}$ additives in the coating solution, are shown in Fig. 2A. The size and density of the clusters have been quantified in Figure S1. Due to the ferromagnetic nature of the CRS substrate, which interfered with electron microscopy imaging, Fe thin films were prepared to further investigate the coating formation mechanism with higher spatial resolution. Fig. 2B shows the pristine Fe thin film (uncoated) alongside the coated films with varying $Cu^{2+}$ concentrations.

The surface morphology of both CRS and Fe thin film substrates changes noticeably with increasing $Cu^{2+}$ concentration. At lower concentrations of 10 ppm, the coating surfaces on both substrates are characterized by small, uniformly distributed clusters with no signs of agglomeration. On Fe thin film, the cluster diameter remains slightly larger (~0.29 μm) compared to CRS (~0.26 μm). The cluster density on CRS is higher, with more clusters evenly spread (~5.56 counts/μm²), while Fe thin film shows a lower count(~1.88 counts/μm²), indicating a denser distribution on CRS. This suggests that the 50 ppm PAMAM chelating agent effectively controlled the Cu deposition on both substrates, but CRS offers a more uniform and dense cluster distribution. The high density of amine and amide functional groups in PAMAM allows it to chelate with $Cu^{2+}$ ions, controlling the amount of Cu deposited in the coating. As the $Cu^{2+}$ concentration increased the surface morphology on both substrates changed slightly, with larger clusters visible on both surfaces. When the $Cu^{2+}$ concentration reaches 20 ppm, larger clusters of ~0.30 μm size are seen on CRS, while the Fe thin film (~0.36 μm) begins to show more pronounced agglomeration. At 40 ppm $Cu^{2+}$, the surface morphology is significantly altered on both CRS and Fe thin film, with bigger size clusters forming and extensive agglomeration becoming evident. Magnified SEM images of Cu20 and Cu40 are shown in Figure S2. The surfaces on both substrates become less homogeneous, and the cluster density decreases significantly (~0.88 counts/μm² on CRS to ~0.55 counts/μm² on Fe). The Fe thin film shows more pronounced inhomogeneity and unevenness than CRS, with agglomeration dominating, as highlighted in the red-circled areas (Fig. 2B). The cluster count on both substrates is at its lowest, but Fe thin film shows larger and fewer clusters than CRS. At this point, the 50 ppm PAMAM may no longer be sufficient to bind the $Cu^{2+}$ ions, leading to uncontrolled Cu deposition and larger agglomerates on both substrates.

The pristine uncoated CRS substrate exhibits unevenly distributed surface defects, while the pristine Fe thin film is less rough. Surface XPS analysis of the pristine Fe thin film confirms the formation of a $Fe_2O_3$ layer, consistent with the observed surface texture and similar to the oxidation patterns typically found in bulk carbon steel substrates (Figure S3) [27]. The rougher surface of the CRS, as seen in Fig. 2A, shows more cracks compared to the smoother uncoated Fe thin film in Fig. 2B. Rough surfaces like CRS provide more defect sites, such as cracks, grain boundaries, and dislocations, which serve as nucleation points for $Cu^{2+}$ ion deposition. These defects lower the energy barrier for nucleation, making it easier for ions to deposit and increasing surface reactivity. Conversely, smoother surfaces are less receptive to coatings, as the literature suggests that surfaces with more indentations and cracks undergo stronger acid reactions, enhancing coating surface bonding [28]. This explains the better coverage of Cu additives on CRS than on Fe thin films.

Although the growth rates differ between substrates, Fe thin films are a good model for analyzing the coating chemistry and internal

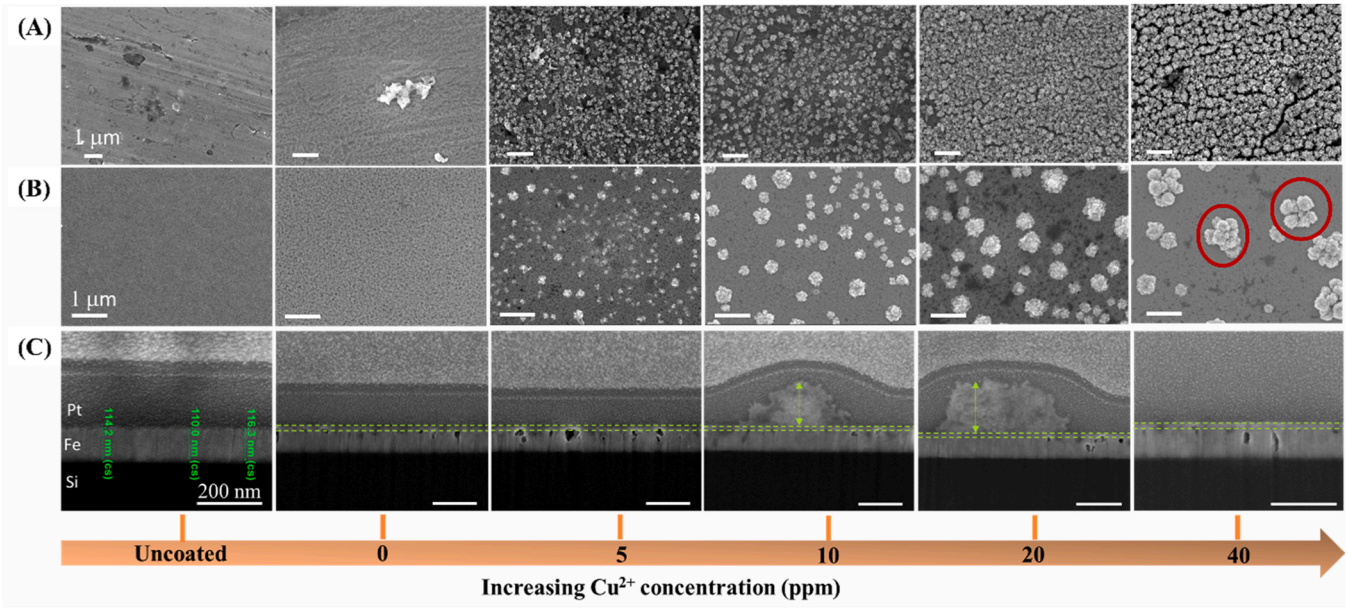


**Fig. 2.** Surface morphology of different coating samples on CRS and Fe thin film substrates with increasing Cu concentration in the coating solution. (A) CRS substrate, (B) Fe thin film, and (C) cross-sectional profiles of the pristine Fe thin film and the coated films are indicated by green dashed lines.

microstructure. Fig. 2C shows the cross-section of the uncoated Fe thin film, which has a uniform thickness of 113 ± 3 nm. The conversion coating layer consistently measures ~20 nm in thickness across all conditions. In the absence of $Cu^{2+}$ (0 ppm), the hybrid coating on the Fe thin films shows no cluster formation but does exhibit voids (Fig. 2C). Intense fluoride ions activate and dissolve the surface upon submersion of the Fe substrate in the solution. These fluoride ions, originating from $H_2ZrF_6$, might interact with the Zr oxide layer, permeating the natural oxide layer on the Fe surface, and resulting in void formation [29]. However, when $Cu^{2+}$ ions are present, its reduction of $Cu^{2+}$ ions to metallic Cu further facilitates the anodic dissolution of Fe [30], explaining the more significant void formation observed with 5 ppm Cu. However, increasing $Cu^{2+}$ concentration can facilitate substrate passivation by forming protective layers such as CuO or $Cu_2O$. This barrier obstructs fluoride ion access to the oxide layer, mitigating localized Fe dissolution and reducing void formation. The oxidation of particles may also occur in the presence of dissolved $O_2$ or NO $[3]^-$ ions, with the role of NO $[3]^-$ ions extensively investigated in recent research [31]. The formation of the Cu oxide layer on the coated samples will be discussed in the following sections.

The size of Cu clusters is also crucial in determining the overall performance of the coating. At a lower $Cu^{2+}$ concentration, smaller Cu clusters form, providing better surface coverage and uniformity, which may enhance adhesion. While, larger aggregates increase surface roughness and non-uniformity, potentially leading to defects such as cracks or delamination. Therefore, optimizing the $Cu^{2+}$ concentration is essential to balancing these effects and ensuring adequate corrosion protection and strong adherence.

### 3.2. *Effect of $Cu^{2+}$ ions on the chemical distribution of the coating and internal cluster formation*

STEM characterization was performed to examine the effect of varying $Cu^{2+}$ ion concentrations on the internal microstructure and chemical distributions within the coated samples. This analysis compares the coating regions with clusters to those without clusters (Fig. 3A-C) as a function of $Cu^{2+}$ additive concentration. The results show that the Cu40 sample contains significantly more Cu in the cluster regions than Cu10 and Cu20. Zr and Cu are present in the cluster regions, while the non-cluster regions primarily consist of Zr, with consistently low Cu

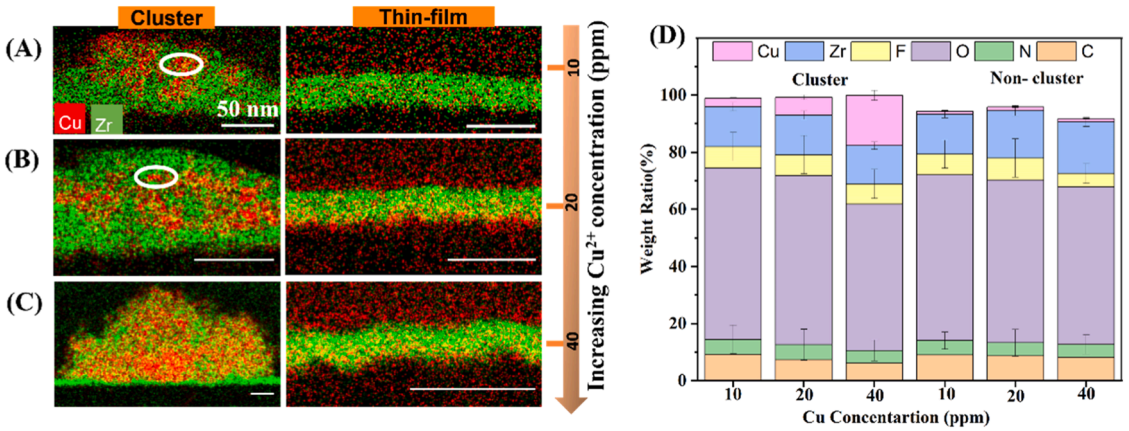


**Fig. 3.** STEM/EDX analysis of coatings with different amounts of $Cu^{2+}$ showing the morphology, elemental distribution, and weight ratio profile. (A) Cu10, (B) Cu20; note the agglomeration of Cu indicated by the white circle, (C) Cu40, and (D) Elemental weight ratio profile on the cluster and non-cluster regions, indicating how Cu accumulates more in clusters as the concentration increases.

content across all $Cu^{2+}$ concentrations.

The internal microstructure of the cluster regions reveals Cu-containing features on the nanometer scale, distributed within a Zr-rich matrix. This structure aligns with previous studies indicating that these clusters have a core-like shape composed of Cu and Zr [25]. The Cu to Zr weight ratio in the cluster and non-cluster region is shown in Fig. 3D, quantitatively supporting the elemental mapping. Specifically, as expected, the Cu40 sample has the highest Cu accumulation in the clusters, with higher $Cu^{2+}$ concentrations in the coating solution. The Cu to Zr weight ratio increases as Cu concentration rises as shown in Figure S4, with the cluster regions becoming more Cu-rich. In contrast, the non-cluster regions maintain a relatively stable Zr-rich composition regardless of the $Cu^{2+}$ concentration in the coating solution.

The critical insight from this analysis is the effect of Cu accumulation within the clusters on the properties of the coating. For the Cu20 sample, a moderate Cu to Zr ratio in the cluster region (0.45:1) suggests a balanced amount of Cu is deposited. In contrast, the higher Cu to Zr ratio in the Cu40 sample (1.32:1) leads to the formation of larger Cu aggregates, as seen in the SEM images (Fig. 2). Literature indicates that when the Cu to Zr weight ratio exceeds 0.7:1, it can form large clusters or agglomerates, reducing uniformity and negatively impacting over time [18]. On the other hand, the non-cluster regions exhibit consistently low Cu to Zr ratios across all samples. This suggests that outside of these clusters, Cu deposition is well-regulated, with Cu being evenly distributed in smaller amounts while the rest of the coating remains Zr-dominant.

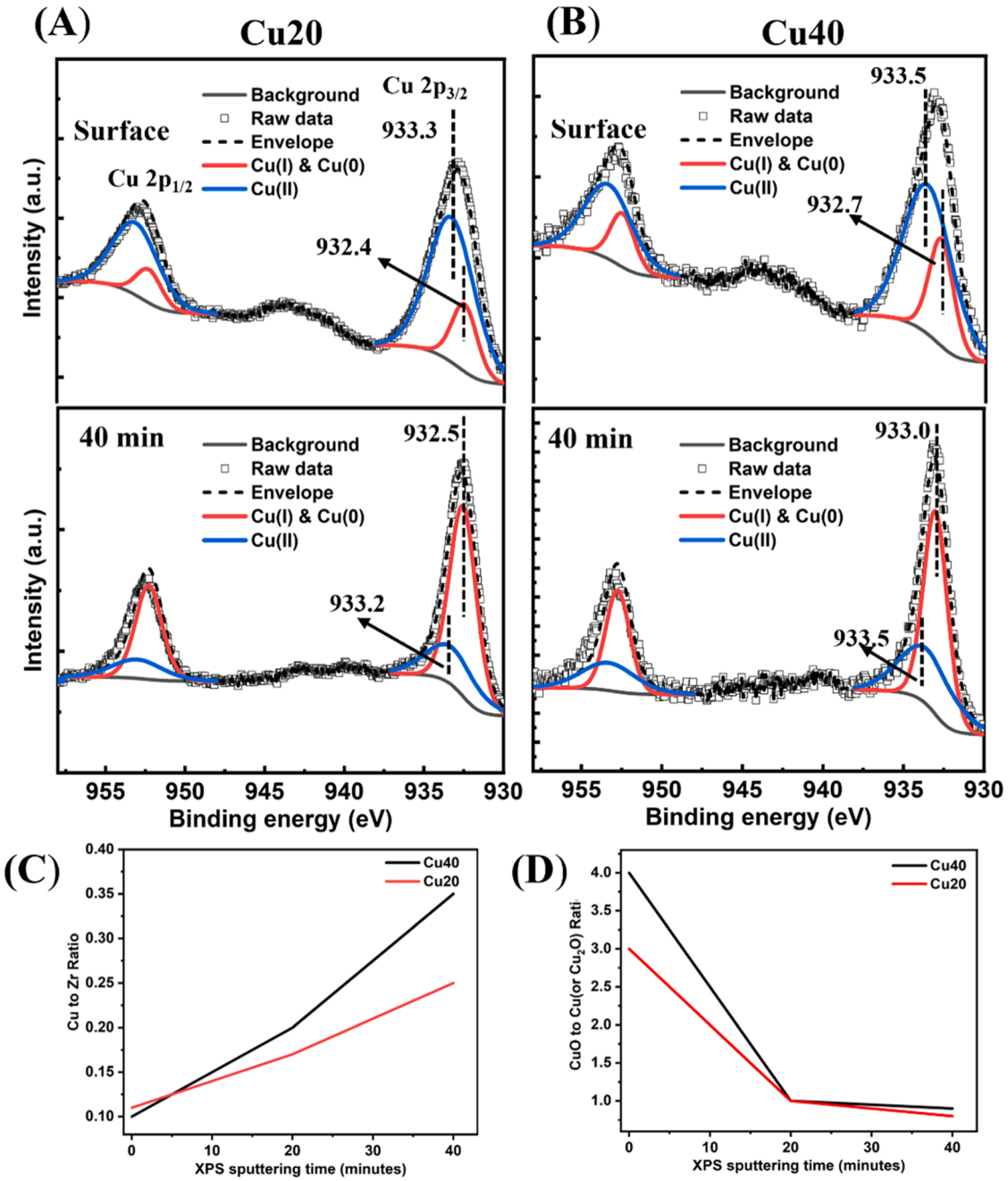


**Fig. 4.** XPS analysis of coated samples at the surface and after 40 min of Ar sputtering. (A) Cu20, (B) Cu40, (C) Cu to Zr weight ratio profile, and (D) CuO to Cu (or $Cu_2O$) weight ratio analysis at different sputtering times.

### 3.3. Evolution of atomic ratio and chemical composition along the depth direction

The utilization of XPS provided detailed insights into the variations in chemical composition with different concentrations of Cu. Specifically, the investigation focused on how these variances affect the formation and distribution of Cu compounds throughout the coating layers. To determine the Cu oxidation states at the surface and in the inner region, the Cu 2p XPS peaks for Cu20 and Cu40 were deconvoluted. Fig. 4A-C shows the Cu 2p fitted XPS spectra of Cu20, and Cu40 samples at the surface and with 40 min of Ar sputtering.

The fitting parameters for Cu $2p_{3/2}$ in Cu20 and Cu40 are detailed in the Table S1. In XPS, more extended Ar sputtering periods progressively remove surface material, allowing investigation into deeper coating layers. Figure S5 shows the XPS spectra from Cu20 and Cu40 samples sputtered for 20 mins. At the surface (0 min sputtering), the Cu $2p_{3/2}$ peak for both Cu20 and Cu40 is identified at 933.3 ± 0.1 eV, accompanied by a satellite peak near ~942.0 eV, characteristic of Cu(II) oxide (CuO) [32], indicating a higher oxidation state of Cu at the surface. After 40 min of sputtering, however, the peak shifts to 932.5 ± 0.1 eV, corresponding to Cu(0) or Cu(I). This shift suggests a reduction in the oxidation state of Cu as the analysis moves deeper into the coating. As shown in Table S2, the area and % concentration of the Cu(II) component are higher at the surface (0 min sputtering) for both samples compared to after 40 min of sputtering. Conversely, the concentration of Cu(0) or Cu(I) increases as the XPS analysis progresses towards the coating-Fe interface. Notably, after 40 mins of sputtering, both samples exhibit a decrease in the Cu(II) signal; however, Cu40 appears to retain more Cu(II) than Cu20, as indicated by the % concentration column in Table S2. This observation could imply that the CuO layer in Cu40 is thicker and is present in a slightly deeper region of the coating than in Cu20. The comparison between Cu20 and Cu40 indicates that Cu40 retains a stronger CuO signal even after sputtering, suggesting more pronounced surface oxidation in Cu40.

The concentration of Cu in the coatings did not directly alter their chemical characteristics. Oxidized Cu species on the surface could arise from two different plausible processes. The first involves directly incorporating Cu(II) ions from the treatment solution. Alternatively, these oxidized states could result from the subsequent oxidation of initially deposited elemental Cu(0). During the cathodic reduction in the coating deposition, $Cu^{2+}$ ions gain electrons, converting to metallic Cu(0) through the reaction: $Cu^{2+} + 2e^- \rightarrow Cu$. These Cu particles could then undergo oxidation in the presence of dissolved $O_2$ or $NO_3^-$ ions. Notably, recent studies have highlighted the role of nitrate ions in facilitating such oxidation processes, potentially leading to the formation of CuO [20,25]. The higher amount of metallic Cu or $Cu_2O$ in the thin film compared to the surface suggests a gradient in $O_2$ availability, which inherently limits the extent of further oxidation within the coating. Given the complex interplay of chemical and electrochemical reactions in this system and the variety of Cu species identified, the second hypothesis—that Cu(0) undergoes oxidation after deposition—appears more plausible for explaining the predominance of detected Cu(II).

Furthermore, the Cu to Zr atomic ratio analysis at different sputtering times highlighted another aspect of the chemical behavior of the coating. Fig. 4C and D show the Cu to Zr and CuO to Cu (or $Cu_2O$) ratios for Cu20 and Cu40 at various sputtering times, respectively. As sputtering time increased, the Cu to Zr ratio also increased from the surface to the inner regions of the coatings, indicating that Cu species formation is more dominant in the initial stages of the coating process. This trend was observed in both Cu20 and Cu40 samples. Additionally, the Cu40 sample, which had a higher concentration of $Cu^{2+}$ ions in the solution, exhibited a higher Cu to Zr ratio than Cu20, suggesting that more Cu was deposited on the substrate when a higher concentration of $Cu^{2+}$ ions was present. The CuO to Cu (or $Cu_2O$) ratio decreased from the surface to the inner layers, further supporting the reduction in the oxidation state of Cu as the analysis moved deeper into the coating. This trend is consistent with observations in many studies of Cu-based coatings or oxides, where CuO is typically found on the surface due to its higher stability in the presence of oxygen, while $Cu_2O$ (Cu(I)) and metallic Cu are more common in the subsurface or bulk regions where $O_2$ penetration is limited [32–35]. The higher initial CuO to Cu (or $Cu_2O$) ratio observed at the surface in Cu40 indicates that surface passivation is more pronounced than Cu20.

CuO is well-documented for its corrosion-resistant properties, primarily because it forms a passivation layer that protects the underlying metal from further oxidation [36]. This suggests that the Cu40 coating may offer better initial oxidation resistance due to a thicker or more extensive oxide layer on the surface, which could act as a protective barrier [37]. The study revealed a layered, where clusters were found to have a core of metallic Cu surrounded by an oxidized exterior.

### 3.4. Surface morphology and Cu compositions change of the coating in NaCl solution

The behavior of Cu and Zr in response to NaCl exposure provides critical insights into the performance of these conversion coatings under saline conditions. The influence of NaCl on the internal microstructure and chemical distribution was characterized by STEM/EDX analysis. In the Cu10 sample (Fig. 5A), a notable difference is observed in the morphology of the coatings before saline and after immersion in NaCl for 24 h. Before treatment, the clustered regions exhibit a homogeneous distribution of Cu and Zr. After exposure to NaCl, the selective dissolution of Cu becomes evident, leaving behind a predominantly Zr-based matrix.

The dissolution of Cu from these regions indicates its susceptibility in chloride-rich environments while Zr remains intact, protecting against further corrosion. Zr, known for its strong affinity for oxygen, forms a stable, dense, and impermeable oxide layer ($ZrO_2$) on its surface when exposed to air or water [38]. Cu is a reactive metal that readily undergoes oxidation in the presence of chloride ions [39]. The decrease in Cu weight percentage after immersion may indicate the formation of corrosion products. Additionally, Fe redeposition was observed on the surface of the coating after treatment. When the Fe substrate interacts with NaCl, the chloride ions ($Cl^-$) play a crucial role due to their aggressive nature, particularly in penetrating protective oxide layers. However, in this case, the $ZrO_2$ layer remained relatively stable in the saline environment, preventing $Cl^-$ ions from penetrating the protective barrier. The attack appears to originate from the backside of the substrate, as the Fe thin film was deposited on a Si wafer. Some solution may have seeped through defects that likely arose during the deposition process, allowing it to reach the substrate and partially dissolve the Fe layer. This dissolution suggests that Fe may be oxidized to $Fe^{2+}$ ions at anodic areas on the metal surface, releasing electrons. Oxygen is reduced in water at cathodic areas, and these electrons produce hydroxide ions. These hydroxide ions combine with $Fe^{2+}$ to form Fe(II) hydroxide, which, with sufficient oxygen, transforms into magnetite, a more stable corrosion product [40,41]. The resulting Fe oxides can then travel through the solution and may redeposit onto the surface of the coating, forming a new layer atop the original coating [42]. This process is evident in Cu10 and Cu40 samples (Fig. 5B), where Fe redeposition is visible on the surface post-immersion. Figure S6 further quantifies this phenomenon, showing that post-immersion, the Cu to Zr weight ratio in both the clustered and non-clustered regions approaches zero. The significant reduction in Cu content across the coating corroborates the EDS results, which reveal the near-complete dissolution of Cu from the coating after 24 h in the NaCl solution.

### 3.5. In situ XRF microscopy and XANES analysis of concentration evolution of the coating in NaCl solution

*In situ,* XRF microscopy and XANES studies were conducted to elucidate further the chemical changes occurring within the coating

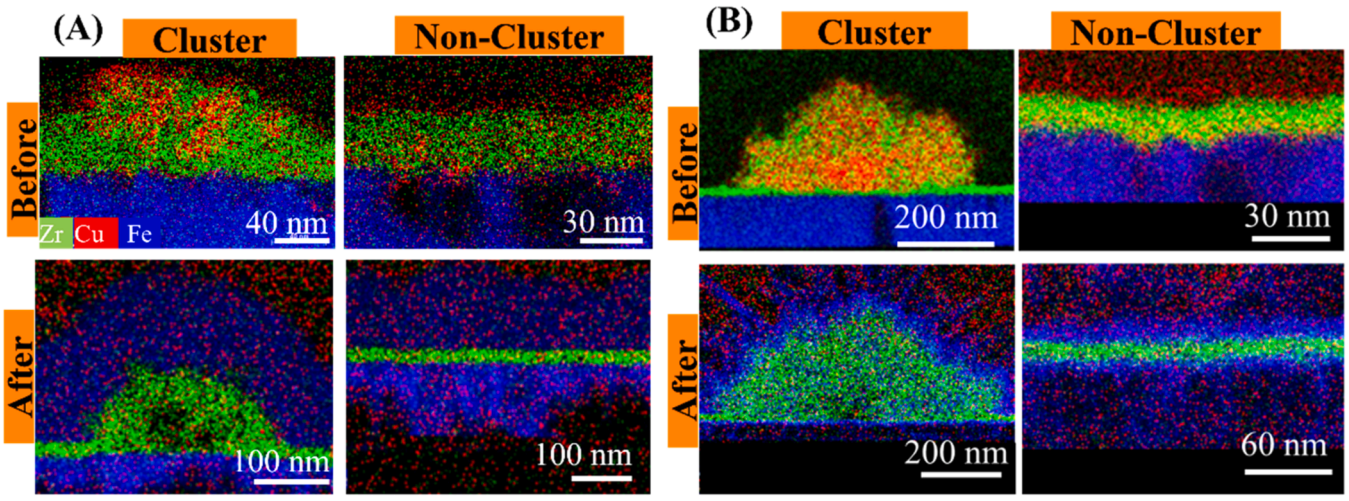


**Fig. 5.** STEM/EDX analysis of coatings before and after NaCl solution immersion in cluster and non-cluster areas. (A) Cu10, and (B) Cu40.

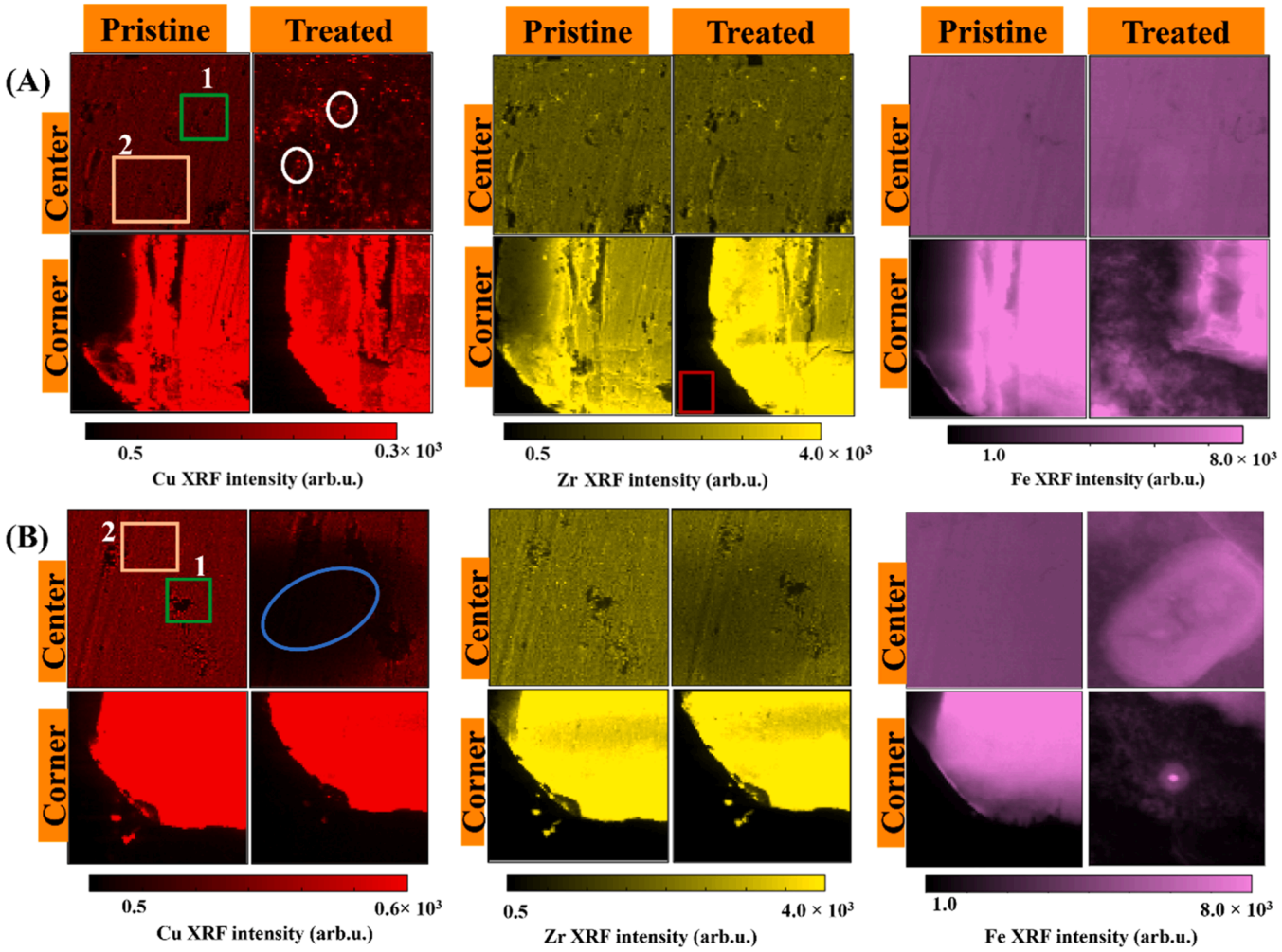


**Fig. 6.** XRF mapping of Cu, Zr, and Fe distribution before and after NaCl immersion in the central and corner regions of the samples. (A) Cu20 sample, and (B) Cu40 sample. The green and orange highlighted areas in (A) and (B) represent specific small ROIs designated SROI 1 and SROI 2 for in-depth analysis. These SROIs are depicted in Figure S7 and Figure S8A for Cu20 and Figure S9 and Figure S10A for Cu40, respectively, for a comprehensive elemental comparison. Some agglomerated Cu species are highlighted in white circles in (A). The blue circle in (B) marks the area showing the removal of Cu. The red inset refers to the location where fluorescence counts were collected from the solution region, with results shown in Figure S11A.

during NaCl exposure. The Cu20 and Cu40 samples were compared to gain insights into how varying Cu concentrations influence the protective efficacy of the coatings against salt-induced corrosion. Fig. 6A shows the XRF mapping of Cu, Zr, and Fe in the Cu20 sample, highlighting differences between the pristine and treated conditions at both the center and corner of the sample. Qualitatively, Cu clusters were reduced in the central region after NaCl immersion compared to the pristine state. This reduction indicates that Cu dissolution occurred, leading to the formation of ions or corrosion products, redeposited as agglomerates on the sample, as highlighted by the white circles. The underlying mechanism for this process will be discussed later in this section. In contrast, Zr showed no noticeable alterations in its quantity or structure before and after NaCl treatment.

However, a modest increase in Fe intensity was observed at the center of the sample, likely due to the redeposition of Fe compounds after reacting with NaCl, resulting from an attack on the unprotected backside of the substrate. These findings are consistent with the results from the STEM/EDX analysis. For the Cu40 sample shown in Fig. 6B, Cu counts increased overall in the pristine condition, reflecting the higher concentration of $Cu^{2+}$ ions in the coating solution than Cu20. After NaCl treatment, a significant decrease in Cu XRF counts was noted, particularly in the regions highlighted by the blue circle, indicating the loss of Cu additives. However, unlike in Cu20, no signs of agglomeration were found in Cu40. Similar to Cu20, Zr showed no changes in Cu40 as well.

The *in situ* XRF maps in Fig. 7A illustrate the evolution of Cu distribution in the Cu20 sample during NaCl treatment. Each map

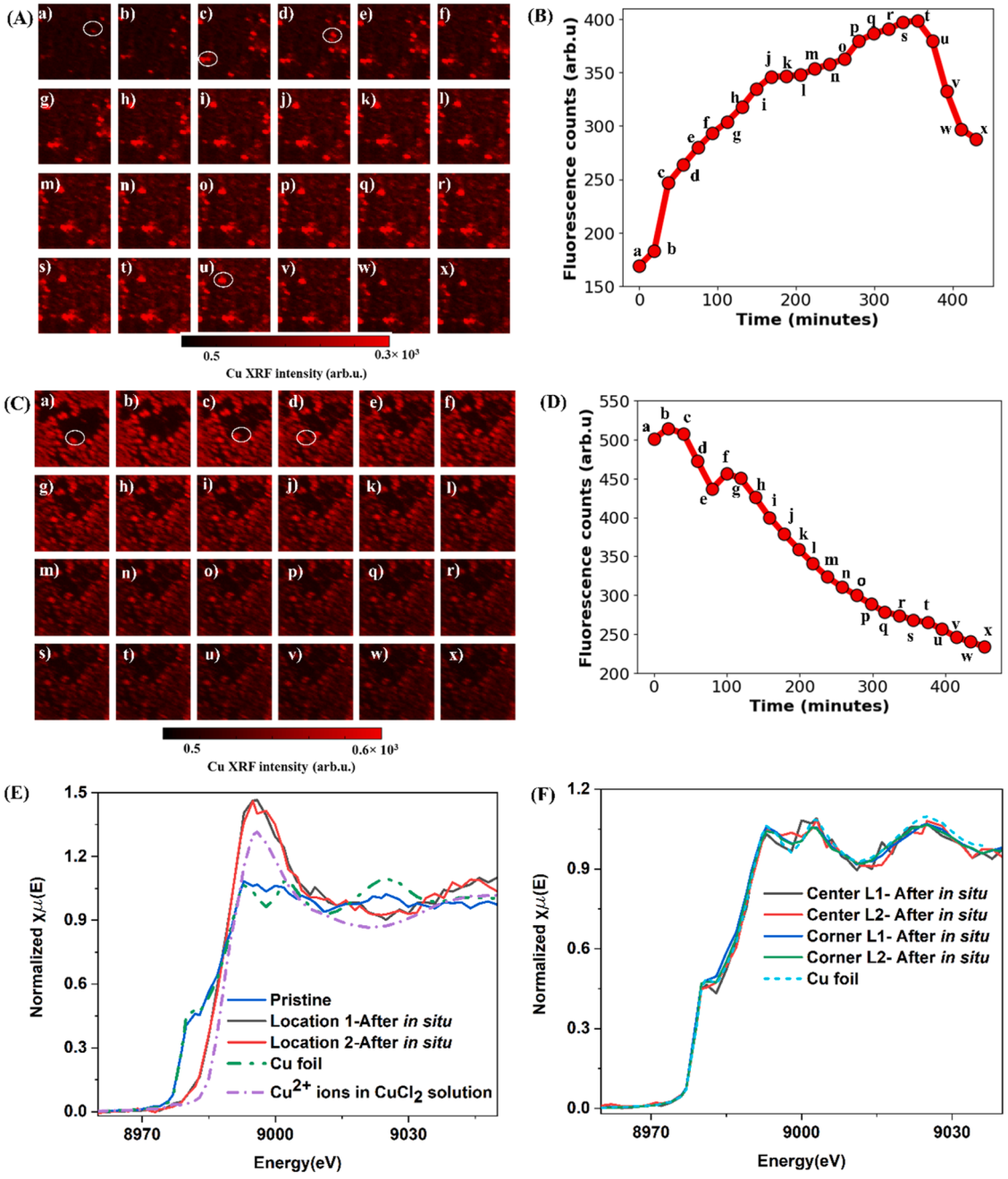


**Fig. 7.** *In situ* monitoring of the Cu and its morphological changes in 3.5 wt.% NaCl for 500 mins using XRF microscopy and XANES. (A) and (C) *In situ* XRF maps for Cu20 and Cu40 samples, respectively, showing the morphological changes of Cu. White circles indicate notable aggregations of Cu, (B) and (D) Corresponding time evolution graphs displaying the total XRF fluorescence counts of Cu as a function of time for each XRF map in (A) and (C), respectively; each data point, labeled a - x, corresponds directly to the respective subpanels in (A) and (C). (E) XANES of Cu20 at center, and (F) XANES of Cu 40 at center and corner locations.

corresponds to a specific time point in the evolution profile shown in Fig. 7B, which tracks Cu counts over time. The green inset in Figure S8A indicates where the *in situ* XRF maps for all elements were collected, while the white inset marks the sample region where fluorescence counts were gathered, with results detailed in Figure S11B. An overview of the *in situ* XRF mapping location is provided in Figure S8B.

Initially, Cu counts were low, but as time progressed, the counts and the size of Cu clusters increased (see maps 'a' and 'i' in Fig. 7A). These clusters, highlighted with white circles, later decreased both count and size (compare maps 's' and 'x'). This behavior suggests a dynamic process where Cu was initially dissolved into the solution and redeposited at the center. The cyclical pattern of Cu concentration observed supports a recurring mechanism of dissolution and redeposition. This is further corroborated by the evolution of Cu counts in the solution and sample regions, as shown in Figure S11A and B. Initially, the Cu concentration in the solution region was higher, decreasing around 100 min before rising again. Conversely, in the sample region (Figure S11B), Cu concentrations were low initially but increased after 100 min, indicating redeposition onto the sample surface. This cyclical variation in Cu distribution strongly suggests a repeated dissolution-redeposition mechanism: Chloride ions can cause significant corrosion in Cu because they tend to create an unstable layer of Cu(I) chloride (CuCl) and form soluble complexes such as Cu(II) chloride ($CuCl_2$) and Cu(I) chloride ($CuCl_3^{2-}$) [43]. Cu undergoes a dissolution-precipitation process, forming Cu(II) chloride ($CuCl_2$) [44]. In chlorinated environments, the typical reaction that occurs on the surface of Cu is the reduction of oxygen, which is the cathodic processes described by reaction1 (R1). This typically results in a slight elevation in the pH of the solution. On the anodic side, the oxidation of metallic Cu to Cu(I) occurs, as shown in R2 [45]. The Cu(I) ions then combine with chloride ions to form an unstable and insoluble layer of CuCl, as represented by the R3. This Cu chloride complex is short-lived and has limited solubility in water. It quickly transitions into a soluble Cu chloride complex, acting as a corrosive agent on the Cu surface. The instability of this layer results in its transformation into a soluble complex $[CuCl_2]^-$, as described by R4. These soluble complexes do not remain on the surface; instead, due to their higher concentration at the surface relative to the bulk solution, they diffuse away into the solution. The soluble CuCl $[2]^-$ can further oxidize into Cu(II) ions via R5, perpetuating the ongoing dissolution of Cu. This mechanism likely explains the cyclic process observed in the Cu deposition and removal.

$$O_2 + 2H_2O + 4e^- \rightarrow 4OH \quad \text{(R1)}$$

$$Cu \rightarrow Cu^+ + e^- \quad \text{(R2)}$$

$$Cu^+ + Cl^- \rightarrow CuCl_{insoluble} \quad \text{(R3)}$$

$$CuCl_{insoluble} + Cl^- \rightarrow \left[CuCl_2^-\right]_{soluble} \quad \text{(R4)}$$

$$\left[CuCl_2^-\right]_{soluble} \rightarrow Cu^{2+} + 2Cl^- + e^- \quad \text{(R5)}$$

The *in situ* XRF maps of Cu evolution for Cu40 are shown in Fig. 7C. Compared to Cu20, Cu40 exhibited less variation in Cu distribution over time, with no significant morphological changes observed. Although a decrease in Cu was noted over time, as indicated by the time evolution plot in Fig. 7D, a similar cyclic trend of removal and redeposition may also occur in the Cu40 sample. However, due to the higher initial concentration of Cu in the Cu40, these changes likely take longer to become apparent, suggesting a slower reaction rate in Cu40 than in Cu20.

XANES analysis was performed, with the Cu K-edge spectra for the Cu20 sample shown in Fig. 7E. The initial state of the pristine Cu20 sample indicated a metallic state of Cu, with the XANES spectrum matching that of Cu foil. After 500 min of NaCl exposure, XANES spectra were collected from two locations (L1, L2) in the center of the sample, as marked in Figure S12. Post-treatment analysis revealed changes in the Cu state at the center, prompting further investigation to determine if these changes were due to the formation of Cu compounds such as $CuF_2$, $Cu(OH)_2$, $CuCl_2$, or $Cu^{2+}$ ions. All the Cu standards are shown in Figure S13. The spectra obtained resembled those of $Cu^{2+}$ ions, as depicted in Fig. 7E, which can be explained by the earlier reaction mechanisms (R5). It was concluded that Cu transitioned from the metallic state (0) to the +2 oxidation state following NaCl exposure. In contrast, the XANES spectra for Cu40, shown in Fig. 7F, exhibited no changes in Cu compounds at either the center or corner locations. The post-treatment state remained metallic at both positions, further supporting the slower reaction rate in Cu40, which was also evident in the *in situ* XRF maps. The specific locations where the XANES data were collected after treatment are indicated in Figure S12.

The *in situ* XRF map tracking Zr evolution in the Cu20 sample is presented in Fig. 8A, with the corresponding counts *versus* time plot shown in Fig. 8B.

The XRF maps confirm the stability of Zr, as no changes in its morphology were detected throughout the NaCl immersion. The increase in the Zr signal over time is likely due to the dissolution and diffusion of Cu into the solution, allowing a more significant amount of the X-ray beam to penetrate the Zr-containing coating near the substrate. Furthermore, as Cu attenuates less Zr XRF signal, more Zr signal reaches the detector. For the Cu40 sample, the *in situ* XRF maps are depicted in Fig. 8C, and the associated time evolution is displayed in Fig. 8D. Both the Cu20 and Cu40 samples showed that Zr remained highly stable, with no evident morphological shifts following immersion.

The XANES spectra for Zr at the center of the Cu20 sample (Fig. 8E) align with the $ZrO_2$ standard, confirming that the chemical composition of the coating is $ZrO_2$. This finding is supported by the XPS Zr 3d core level spectrum, presented in Figure S14, which includes a fitting of doublets. The binding energy for the Zr 3d5/2 electron was measured at ~182.7 eV, aligning with the values expected for $ZrO_2$. Consistent with previous findings, $ZrO_2$ remained unchanged after NaCl exposure in the Cu40 sample, as illustrated in Fig. 8F, further confirming the stability of Zr compounds under these conditions.

Fig. 9A presents the *in situ* XRF analysis of Fe within the Cu20 sample over time, with the corresponding Fe fluorescence counts plotted in Fig. 9B. This quantitative data suggests an increase of the Fe signal at the center of the sample, indicating either the exposure of a Fe-rich substrate or the redeposition of Fe compounds on the surface as corrosion products. An XANES analysis was conducted to verify these observations.

Following the *in situ* treatment, XANES analysis of the Cu20 sample center revealed that Fe remained metallic, consistent with the Fe foil standard (Fig. 9E). This suggests that the Fe in these regions did not undergo oxidation and was effectively protected by the $ZrO_2$ layer. However, at the corners of the sample, the formation of $Fe_2O_3$ was observed. This indicates that corrosion was likely initiated from the unprotected backside of the Fe substrate, where exposure to the saline environment allowed for oxidation over time. The resulting $Fe_2O_3$, formed as a corrosion product, may have migrated through the solution and deposited onto the surface. Similarly, the Cu40 sample (Fig. 9F) exhibited a non-uniform distribution of Fe across the sample. Both the corner and center locations displayed heterogeneity, with a mixture of Fe and $Fe_2O_3$ in different areas. This non-uniformity can be attributed to the backside attack mechanism discussed for Cu20, where $Fe_2O_3$ forms and migrates to the surface. At the same time, the Fe directly beneath the $ZrO_2$ layer remains protected in its metallic state.

### 3.6. Electrochemical analysis of Cu20 and Cu40

To further elucidate the electrochemical stability and corrosion resistance of Cu-incorporated Zr-based conversion coatings, PDP measurements were conducted on Cu20, and Cu40 samples (Fig. 10). The PDP curves provide further insight into the corrosion mechanisms of Cu20 and Cu40 coatings. The corrosion potential ($E_{corr}$) and corrosion current density ($I_{corr}$) from PDP results serve as critical indicators of the thermodynamic stability and kinetic corrosion rates, respectively, and

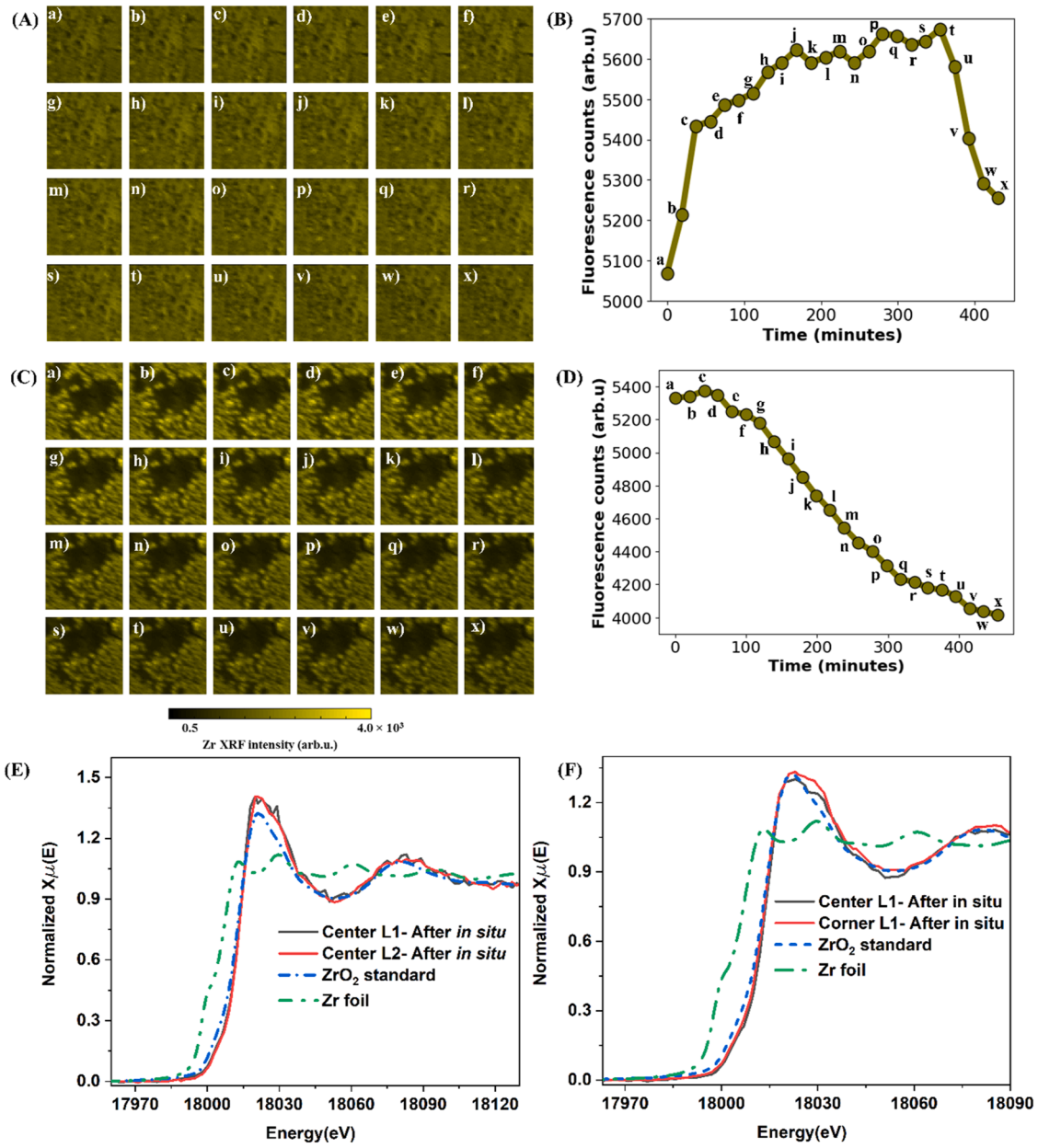


**Fig. 8.** *In situ* monitoring of the Zr and its morphological changes in 3.5 wt% NaCl for 500 min using XRF microscopy and XANES. (A) and (C) *In situ* XRF maps for Cu20 and Cu40 samples, respectively, showing the morphological changes of Zr, (B) and (D) Corresponding time evolution graphs displaying the total XRF fluorescence counts of Zr as a function of time for each XRF map in (A) and (C), respectively; each data point, labeled a - x, corresponds directly to the respective subpanels in (A) and (C), (E) XANES of Cu20 at the center, and (F) XANES of Cu 40 at the center and corner location.

were obtained from the PDP results using Tafel plots (Table S3). The Cu20 exhibited the most negative $E_{corr}$ value, signifying its high susceptibility to corrosion in chloride-rich environments. Furthermore, its $I_{corr}$ value was higher than that of the Cu40, confirming an accelerated corrosion rate. In contrast, Cu40 coatings exhibited a shift towards a more positive $E_{corr}$, indicating enhanced thermodynamic stability and resistance to electrochemical dissolution. Cu40 displayed the highest $E_{corr}$ and the lowest $I_{corr}$.

The electrochemical differences between Cu20 and Cu40 coatings also correlate with the dissolution-redeposition mechanisms observed via *in situ* XRF and XANES studies. The higher $I_{corr}$ in Cu20 indicates a faster dissolution rate of Cu clusters, leading to a dynamic process where Cu species dissolve into the electrolyte and partially redeposit. This is corroborated by *in situ* XRF, which revealed periodic fluctuations in Cu concentration over time, suggesting a continuous cycle of Cu dissolution and redeposition. Conversely, Cu40 demonstrated a more stable Cu distribution, with no significant redeposition cycles observed, indicating that Cu clusters in Cu40 remain more chemically stable and less prone to dissolution.

While Cu20 provides some level of corrosion protection, its susceptibility to faster Cu dissolution limits its long-term durability. In contrast, Cu40, with lower $I_{corr}$, and stable Cu oxide formation, offers enhanced corrosion resistance in chloride-rich conditions. Future studies could be further conducted with electrochemical processes and kinetic factors influencing the Cu behaviors, coupled with the synchrotron analysis.

The surface morphology of the NaCl-treated samples was characterized by SEM analysis, as shown in Figure S15. In Figure S15A, the Cu20 sample exhibited the presence of cracks, along with white flake-like reaction products deposited on the surface, indicating the

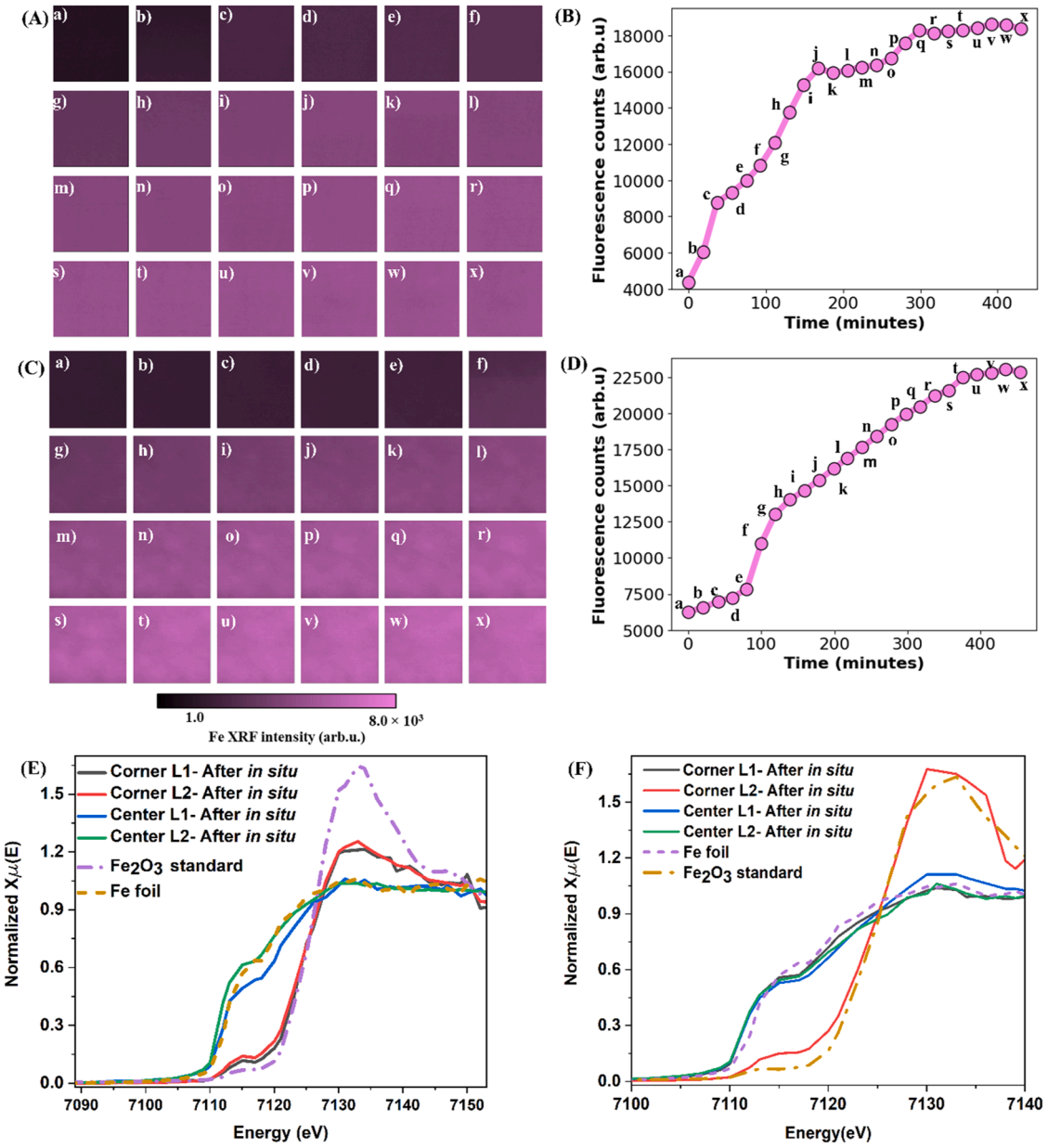


**Fig. 9.** *In situ* monitoring of the Fe and its morphological changes in 3.5 wt.% NaCl for 500 min using XRF microscopy and XANES. (A) and (C) *In situ* XRF maps for Cu20 and Cu40 samples, respectively, showing the morphological changes of Fe, (B) and (D) Corresponding time evolution graphs displaying the total XRF fluorescence counts of Fe as a function of time for each XRF map in (A) and (C), respectively; each data point, labeled a - x, corresponds directly to the respective subpanels in (A) and (C), (E) XANES of Cu20 both at the center and corner, and (F) XANES of Cu 40 at the center and corner location.

disintegration of the Cu clusters. These findings are consistent with the XRF results, which demonstrated changes in the Cu clusters. In contrast, the surface morphology of the Cu40 sample, depicted in Figure S15B, showed less damage to the clusters and a smaller amount of corrosion products deposited on the surface. This observation suggests that the Cu40 sample exhibits more excellent stability in the NaCl environment. The increased stability observed in Cu40 can be attributed to the higher Cu content, which appears to prolong the time required for reactions to occur in the saline environment.

### *3.7. Formation mechanism $ZrO_2$ -based conversion coatings along with $Cu^{2+}$ additive and its behavior in the saline environment*

The proposed formation mechanism for hybrid Zr-based conversion coatings on Fe substrates with varying $Cu^{2+}$ concentrations emphasizes the interaction between $Cu^{2+}$ ions and PAMAM dendrimers. During the conversion process, the Fe substrate is immersed in a fluoride-containing solution, activating the surface by dissolving the existing metal oxide. This increases the pH at the interface, facilitating the deposition of $ZrO_2$ on the surface through the reaction: - $ZrF_6^{2-} + 4OH^- \rightarrow ZrO_2{\cdot}2H_2O + 6F^-$. PAMAM, with its numerous functional amine groups, binds effectively with $Cu^{2+}$ ions, forming stable coordination complexes [46] as illustrated in Fig. 11. The complexation involves $[Cu(H_2O)_6]^{2+}$ transitioning into a coordination bond with the nitrogen atoms in PAMAM. The number of $Cu^{2+}$ ions encapsulated is proportional to the amine groups in the dendrimer. As the PAMAM concentration increases in the solution, more $Cu^{2+}$ ions are encapsulated, improving the control over Cu deposition. This leads to more stable Cu-dendrimer complexes, enhancing the corrosion resistance of the material and coating stability. After complexation, any unbound $Cu^{2+}$ ions undergo rapid reduction at the cathode, forming larger $Cu^0$ clusters: $Cu^0$ clusters ($Cu^{2+}+2e^- \rightarrow Cu^0$). These $Cu^0$ clusters, upon exposure to air, develop a protective oxide

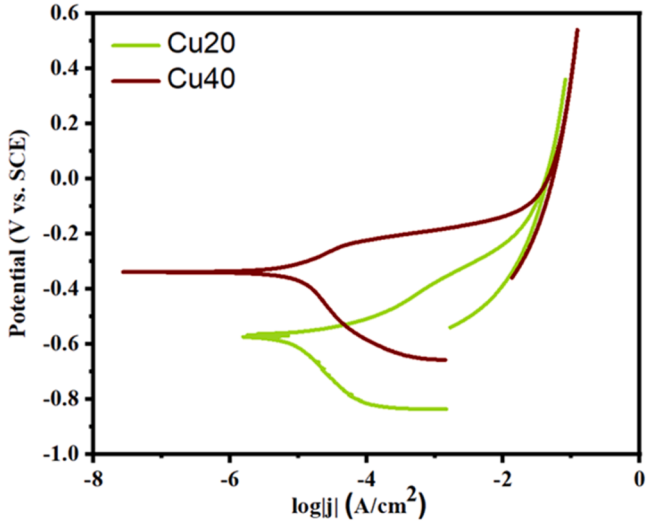


**Fig. 10.** Potentiodynamic polarization curves collected on Cu20 and Cu40.

layer while maintaining Cu⁰ in the inner shell, as evident from Fig. 4. Upon treating the conversion coatings with NaCl, the $ZrO_2$ layer remains intact, acting as a chemical and physical barrier that resists chloride ion penetration, thereby protecting the Fe substrate from corrosion. The stability of $ZrO_2$ against chloride ions is attributed to its dense and tightly packed atomic structure, which prevents ions like $Cl^-$ from penetrating or reacting. Unlike reactive metals, $ZrO_2$ does not form soluble complexes with $Cl^-$ due to its low reactivity and high bond energy, remaining stable under typical NaCl conditions: $ZrO_2 + Cl^- \rightarrow$ No reaction [47]. At lower $Cu^{2+}$ concentrations, Cu oxidizes to Cu⁰ to $Cu^{2+}$, likely through a dissolution-precipitation cycle of diffusible $CuCl_2$: $Cu^0 + 2Cl^- \rightarrow CuCl$ [2]$^-$ where the surface Cu⁰ is converted to $Cu^{2+}$.

$Cu^{2+}$ ions and PAMAM play essential yet distinct roles in forming hybrid Zr-based conversion coatings. PAMAM controls the growth and deposition of Cu clusters by binding to $Cu^{2+}$ ions, ensuring uniform Cu distribution and preventing agglomeration. $Cu^{2+}$ plays a crucial role in the formation of the hybrid conversion coating by influencing the deposition kinetics, morphology, and chemical reactions during the process. It enhances surface characteristics by forming protective oxide layers (CuO) without significantly affecting the overall coating thickness. When complexed with PAMAM, $Cu^{2+}$ undergoes reduced cathodic reactions, which mitigates Fe substrate dissolution and limits the formation of voids beneath the oxide layer. Additionally, $Cu^{2+}$ impacts the precipitation of $ZrO_2$ by altering the pH and regulating the free $Cu^{2+}$ ions in the solution, ultimately enhancing the uniformity of the coating. This balance between surface modification and bulk growth highlights the complementary roles of PAMAM and $Cu^{2+}$ in optimizing the performance of the coating.

## 4. Conclusion

This study demonstrates how organic and inorganic additives influence Zr-based conversion coatings, particularly the role of $Cu^{2+}$ concentration in modifying coating morphology, adhesion, and corrosion resistance. Increasing [$Cu^{2+}$] from 20 to 40 ppm in the treatment solution led to larger cluster diameters and reduced cluster density, with significant agglomeration at higher concentrations due to the limited complexation ability of the 50 ppm PAMAM chelating agent. While $Cu^{2+}$ altered the surface chemistry, it had minimal impact on overall coating thickness under these deposition conditions. Cu20 provided a balance between adhesion and corrosion protection, while Cu40 resulted in excessive Cu agglomeration, potentially affecting adhesion. XPS and STEM/EDX analyses revealed a stratified Cu cluster structure, with an outer CuO layer and a metallic Cu core, which selectively dissolved in NaCl, leaving the Zr oxide layer intact to protect the Fe substrate. XRF and XANES further confirmed that $Cu^{2+}$ plays a key role in corrosion behavior, with Cu20 forming corrosion byproducts, while Cu40 retained more metallic Cu, exhibiting a slower reaction rate. The study highlights the trade-offs between adhesion, surface uniformity, and corrosion resistance, emphasizing the importance of optimizing $Cu^{2+}$ concentration to enhance coating performance. By fine-tuning the relative ratio of Cu additives, the hybrid Zr-based conversion coating benefits from both organic and inorganic additives, offering improved surface properties. This method requires no additional energy, high costs, or complex post-treatments, making it an environmentally friendly, water-based alternative to traditional chromate-based corrosion inhibitors.

## Supporting Information

The diameter of the clusters function of $Cu^{2+}$ concentration (5, 10, 20, and 40 ppm) based on the SEM images of the samples on both the Fe thin film and CRS substrate. XPS of pristine Fe thin film at the surface. Fitting parameters for Cu $2p_{3/2}$ XPS in Cu20 and Cu40. XPS fitting parameters for the different components of the Cu 2p3/2 peak in Cu20 and Cu40. XPS of the coated surface with 20 min Ar sputtering time. Elemental distribution after NaCl treatment for 24 hrs. in the cluster and the non-cluster region for Cu10 and Cu40 samples. XRF of SROI1 for Cu20 sample. XRF mapping of SROI2 in Cu20 sample. XRF SROI1 of Cu40 shows Cu, Zr, and Fe distribution on the coated sample at pristine and treated conditions at the center location. XRF mapping of SROI2 in Cu40 sample. Time evolution plots of Cu20 sample for Cu. Locations

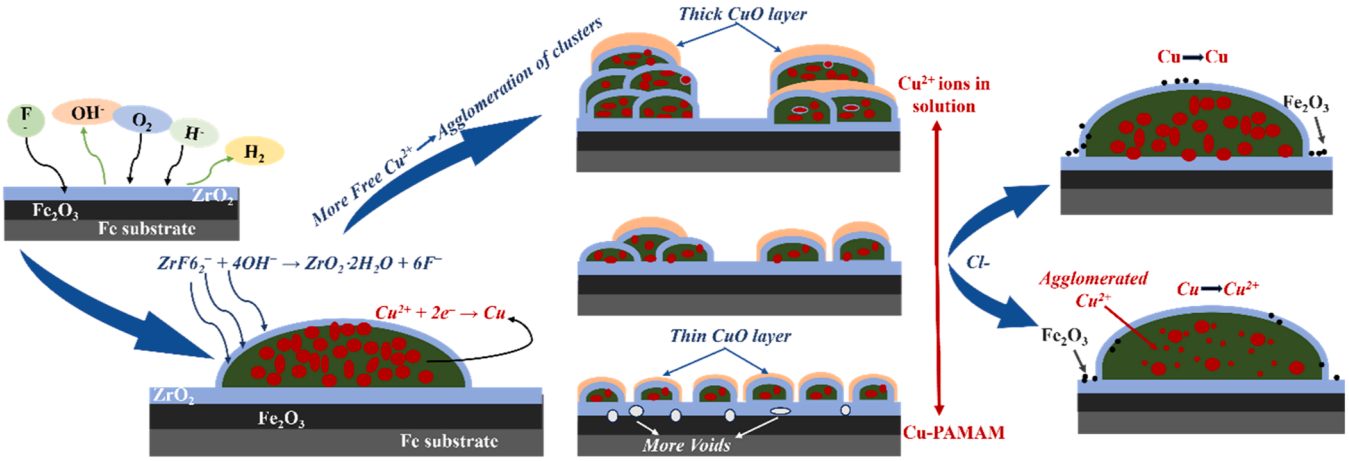


**Fig. 11.** Schematic illustration of the coating formation with $Cu^{2+}$ additives and its variation with different amounts of Cu additives under NaCl conditions.

where Cu, Zr, and Fe XANES were collected for the two different locations for Cu20 (center) and Cu40 (center and corner). Cu standards. Zr 3d XPS peak of samples (A) Cu20, and (B) Cu40 shows the presence of $ZrO_2$. SEM images showing the surface morphology of the samples after 3.5 wt% NaCl treatment. Eq. (R1)-(R5)

## CRediT authorship contribution statement

**Ankita Mohanty:** Writing – original draft, Visualization, Methodology, Investigation, Formal analysis, Data curation, Conceptualization. **Xiaoyang Liu:** Data curation, Conceptualization. **Cheng-Chu Chung:** Data curation. **Donald Vonk:** Writing – review & editing, Conceptualization. **Kim Kisslinger:** Methodology. **Xiao Tong:** Methodology. **Andrew Kiss:** Data curation, Investigation, Methodology, Software. **Gary Halada:** Resources, Conceptualization. **Stanislas Petrash:** Writing – review & editing, Funding acquisition, Conceptualization. **Kate Foster:** Writing – review & editing, Supervision, Project administration, Funding acquisition, Conceptualization. **Yu-chen Karen Chen-Wiegart:** Writing – review & editing, Supervision, Project administration, Data curation, Conceptualization.

## Declaration of competing interest

The authors declare the following financial interests/personal relationships which may be considered as potential competing interests:

Yu-chen Karen Chen-Wiegart reports financial support was provided by Henkel Corporation. If there are other authors, they declare that they have no known competing financial interests or personal relationships that could have appeared to influence the work reported in this paper.

## Acknowledgments

This work was funded by Henkel Corp. under Award 81113. This research used resources and Submicron Resolution X-ray Spectroscopy beamline (SRX, 5-ID) and Beamline for Materials Measurement (BMM, 6-BM)of the National Synchrotron Light Source II, a U.S. Department of Energy (DOE) Office of Science User Facility operated for the DOE Office of Science by Brookhaven National Laboratory under Contract No. DE-SC0012704. This research used resources from the Center for Functional Nanomaterials, which is a U.S. DOE Office of Science Facility, at Brookhaven National Laboratory under Contract DESC0012704. The authors are grateful to Dr. Bruce Ravel (National Institute of Standards and Technology), Lead Beamline Scientist at the BMM beamline, for his expertise and support on XAS characterization at BMM.

## Supplementary materials

Supplementary material associated with this article can be found, in the online version, at doi:10.1016/j.apsadv.2025.100726.

## Data availability

Data will be made available on request.

## References

[1] N.G. Thompson, M. Yunovich, D. Dunmire, Cost of corrosion and corrosion maintenance strategies, Corros. Rev. 25 (3–4) (2007) 247–261.
[2] D.N. Farhey, Structural performance and network dependability of bridge materials in the US, Struc. Eng. Int. 29 (1) (2019) 48–59.
[3] B.X. Wei, J. Xu, Special issue: environmental corrosion of metals and its prevention: an overview and introduction to the Special issue, Coatings (7) (2022) 12.
[4] H.R. Asemani, P. Ahmadi, A.A. Sarabi, H.E. Mohammadloo, Effect of zirconium conversion coating: adhesion and anti-corrosion properties of epoxy organic coating containing zinc aluminum polyphosphate (ZAPP) pigment on carbon mild steel, Progr. Organ. Coatings 94 (2016) 18–27.
[5] S. Adhikari, K.A. Unocic, Y. Zhai, G.S. Frankel, J. Zimmerman, W. Fristad, Hexafluorozirconic acid based surface pretreatments: characterization and performance assessment, Electrochim. Acta 56 (4) (2011) 1912–1924.
[6] W.Q. Zhou, D.Y. Shan, E.H. Han, W. Ke, Structure and formation mechanism of phosphate conversion coating on die-cast AZ91D magnesium alloy, Corros. Sci. 50 (2) (2008) 329–337.
[7] H. Vakili, B. Ramezanzadeh, R. Amini, The corrosion performance and adhesion properties of the epoxy coating applied on the steel substrates treated by cerium-based conversion coatings, Corros. Sci. 94 (2015) 466–475.
[8] I. Milosev, G.S. Frankel, Review-conversion coatings based on zirconium and/or titanium, J. Electrochem. Soc. 165 (3) (2018) C127–C144.
[9] S.H. Wang, C.S. Liu, L. Wang, in: In *A comparative study of zirconium-based coating on cold rolled steel*, International Conference on Advanced Engineering Materials and Technology (AEMT2011), Sanya, PEOPLES R CHINA, Jul 29-31, 2011, pp. 47–52. Sanya, PEOPLES R CHINA.
[10] T. Lostak, S. Krebs, A. Maljusch, T. Gothe, M. Giza, M. Kimpel, J. Flock, S. Schulz, Formation and characterization of $Fe^{3+}/Cu^{2+}$-modified zirconium oxide conversion layers on zinc alloy coated steel sheets, Electrochim. Acta 112 (2013) 14–23.
[11] M. Sababi, H. Terryn, J.M.C. Mol, The influence of a Zr-based conversion treatment on interfacial bonding strength and stability of epoxy coated carbon steel, Progr. Organic Coat.s 105 (2017) 29–36.
[12] F. Andreatta, A. Lanzutti, L. Paussa, L. Fedrizzi, Addition of phosphates or copper nitrate in a fluotitanate conversion coating containing a silane coupling agent for aluminium alloy AA6014, Progr. Organic Coat. 77 (12) (2014) 2107–2115.
[13] B. Ramezanzadeh, M.M. Attar, Effects of Co(II) and Ni(II) on the surface morphology and anticorrosion performance of the steel samples pretreated by Cr (III) conversion coating, Corrosion 68 (1) (2012).
[14] C.S. Velasquez, E.P.S. Pimenta, V.F.C. Lins, Anticorrosive behavior and porosity of tricationic phosphate and zirconium conversion coating on galvanized steel, J. Mater. Eng. Perform. 27 (5) (2018) 2138–2147.
[15] H.R.P. Cardoso, C. Rapacki, J.Z. Ferreira, Monitoring of a Zr-based conversion coating on galvanised steel and its performance against corrosion, Corros. Eng. Sci. Technol. 54 (8) (2019) 726–730.
[16] M. Becker, Chromate-free chemical conversion coatings for aluminum alloys, Corros. Rev. 37 (4) (2019) 321–342.
[17] F.O. George, P. Skeldon, G.E. Thompson, Formation of zirconium-based conversion coatings on aluminium and Al-Cu alloys, Corros. Sci. 65 (2012) 231–237.
[18] D.R. Vonk, I.T.S. Smith, A. BOBADILLA, Thin Corrosion Protective Coatings Incorporating Polyamidoamine Polymers, Google Patents, 2021.
[19] X.Y. Liu, D. Vonk, H. Jiang, K. Kisslinger, X. Tong, M.Y. Ge, E. Nazaretski, B. Ravel, K. Foster, S. Petrash, Y.C.K. Chen-Wiegart, Environmentally friendly Zr-based conversion nanocoatings for corrosion inhibition of metal surfaces evaluated by multimodal X-ray analysis, Acs Appl. Nano Mater. 2 (4) (2019) 1920–1929.
[20] A. Sarfraz, R. Posner, M.M. Lange, K. Lill, A. Erbe, Role of intermetallics and copper in the deposition of $ZrO_2$ conversion coatings on AA6014, J. Electrochem. Soc. 161 (12) (2014) C509–C516.
[21] M.H. Shahini, H.E. Mohammadloo, B. Ramezanzadeh, Recent advances in steel surface treatment via novel/green conversion coatings for anti-corrosion applications: a review study, J. Coat. Technol. Res. 19 (1) (2022) 159–199.
[22] D.R. Vonk, E. Kapic, M.L. Sienkowski, Metal Pretreatment Composition Containing Zirconium, Copper, and Metal Chelating Agents and Related Coatings On Metal Substrates, 580, 2017, p. 813B2. US 9.
[23] C.F. Glover, M.L.C. Lim, J.R. Scully, M. Minerals, S. Mat, in: *The Effect of Surface Treatment on the Performance of a Zirconium-Based Conversion Coating on AA7075 Automotive Alloys for Protection Against Filiform Corrosion*, Nanoscience and Nanotechnology in Advanced Composites Symposium held at TMS 149th Annual Meeting and Exhibition, San Diego, CA, Feb 23-27, 2020, pp. 937–946. San Diego, CA.
[24] T. Ratkevicius, A. Laurinavicius, F. Tuminiene, J. Braduliene, in: *Reduction of negative impact of salts used for winter road maintenance on the environment*, 9th International Conference on Environmental Engineering (ICEE), Vilnius, LITHUANIA, May 22-23, 2014. Vilnius, LITHUANIA.
[25] J. Cerezo, I. Vandendael, R. Posner, J.H.W. de Wit, J.M.C. Mol, H. Terryn, The effect of surface pre-conditioning treatments on the local composition of Zr-based conversion coatings formed on aluminium alloys, Appl. Surf. Sci. 366 (2016) 339–347.
[26] X. Liu, D. Vonk, H. Jiang, K. Kisslinger, X. Tong, M. Ge, E. Nazaretski, B. Ravel, K. Foster, S. Petrash, Y.-C.K. Chen-Wiegart, Environmentally friendly Zr-based conversion nanocoatings for corrosion inhibition of metal surfaces evaluated by multimodal X-ray analysis, ACS Appl. Nano Mater. 2 (4) (2019) 1920–1929.
[27] A.A. Tahir, K.G.U. Wijayantha, S. Saremi-Yarahmadi, M. Mazhar, V. McKee, Nanostructured ($\alpha$-$Fe_2O_3$ thin films for photoelectrochemical hydrogen generation, Chem. Mater. 21 (16) (2009) 3763–3772.
[28] T. Narayanan, Surface pretreatment by phosphate conversion coatings - A review, Rev. Advanced Mater. Sci. 9 (2) (2005) 130–177.
[29] X.Y. Liu, D. Vonk, K. Kisslinger, X. Tong, G. Halada, S. Petrash, K. Foster, Y.C. K. Chen-Wiegart, Unraveling the formation mechanism of a hybrid Zr-based chemical conversion coating with organic and copper compounds for corrosion inhibition, ACS Appl. Mater. Interfaces 13 (4) (2021) 5518–5528.
[30] E. Mysliu, K.S. Storli, H.M. Skogoy, S. Kubowicz, I.H. Svenum, O. Lunder, A. Erbe, Effect of Cu2+on deposition mechanism and structure of ZrO2-based conversion coatings on AA6060 aluminium alloys and their susceptibility to filiform corrosion, Electrochim. Acta 477 (2024) 15.

[31] J. Han, D. Thierry, K. Ogle, Zr-based conversion coating on Zn and Zn-Al-Mg alloy coating: understanding the accelerating effect of Cu(II) and $NO^{3-}$, Surf. Coat. Technol. (2020) 402.
[32] S. Poulston, P.M. Parlett, P. Stone, M. Bowker, Surface oxidation and reduction of CuO and Cu2O studied using XPS and XAES, Surf. Interf. Analy. 24 (12) (1996) 811–820.
[33] H. Bubert, E. Grallath, A. Quentmeier, M. Wielunski, L. Borucki, Comparative investigation on copper oxides by depth profiling using xps, rbs and gdoes, Fresenius J. Analy. Chem. 353 (3–4) (1995) 456–463.
[34] J. Aromaa, M. Kekkonen, M. Mousapour, A. Jokilaakso, M. Lundstroem, The oxidation of copper in air at temperatures up to 100°C, Corros. Mater. Degrad. 2 (4) (2021) 625–640.
[35] S. Choudhary, J.V.N. Sarma, S. Pande, S. Ababou-Girard, P. Turban, B. Lepine, S. Gangopadhyay, Oxidation mechanism of thin Cu films: a gateway towards the formation of single oxide phase, AIP Adv. 8 (5) (2018).
[36] M. Eskandari, A. Shanaghi, M. Kamani, M.A. Niari, Effect of nano-metal oxides (ZnO, $Al_2O_3$ CuO, and $TiO_2$ on the corrosion behavior of a nano-metal oxide/epoxy coating applied on the copper substrate in the acidic environment, Appl. Nanosci. 11 (5) (2021) 1605–1615.
[37] J. Peng, B.L. Chen, Z.C. Wang, J. Guo, B.H. Wu, S.Q. Hao, Q.H. Zhang, L. Gu, Q. Zhou, Z. Liu, S.Q. Hong, S.F. You, A. Fu, Z.F. Shi, H. Xie, D.Y. Cao, C.J. Lin, G. Fu, L.S. Zheng, Y. Jiang, N.F. Zheng, Surface coordination layer passivates oxidation of copper, Nature 586 (7829) (2020) 390. -+.
[38] M. Behzadnasab, S.M. Mirabedini, K. Kabiri, S. Jamali, Corrosion performance of epoxy coatings containing silane treated $ZrO_2$ nanoparticles on mild steel in 3.5% NaCl solution, Corros. Sci. 53 (1) (2011) 89–98.
[39] E.J. Schindelholz, H. Cong, C.F. Jove-Colon, S. Li, J.A. Ohlhausen, H.K. Moffat, Electrochemical aspects of copper atmospheric corrosion in the presence of sodium chloride, Electrochim. Acta 276 (2018) 194–206.
[40] Y.B. Tang, L. Liu, Y. Li, F.H. Wang, Evidence for the occurrence of electrochemical reactions and their interaction with chemical reactions during the corrosion of pure Fe with solid NaCl deposit in water vapor at 600°C, Electrochem. Commun. 12 (2) (2010) 191–193.
[41] E.S.M. Sherif, Corrosion and Corrosion inhibition of pure iron in neutral chloride solutions by 1,1′-thiocarbonyldiimidazole, Int. J. Electrochem. Sci. 6 (8) (2011) 3077–3092.
[42] L. Cáceres, T. Vargas, L. Herrera, Influence of pitting and iron oxide formation during corrosion of carbon steel in unbuffered NaCl solutions, Corros. Sci. 51 (5) (2009) 971–978.
[43] A.M. Alfantazi, T.M. Ahmed, D. Tromans, Corrosion behavior of copper alloys in chloride media, Mater. Des. 30 (7) (2009) 2425–2430.
[44] J. Crousier, L. Pardessus, J.P. Crousier, Voltammetry study of copper in Chloride solution, Electrochim. Acta 33 (8) (1988) 1039–1042.
[45] S. Gudic, L. Vrsalovic, A. Radeljic, E.E. Oguzie, I. Ivanic, S. Kozuh, M. Gojic, Comparison of corrosion behavior of copper and copper alloys in aqueous chloride solution, Chem. Indust. Chem. Eng. Quart. 27 (4) (2021) 383–394.
[46] R.M. Crooks, M.Q. Zhao, L. Sun, V. Chechik, L.K. Yeung, Dendrimer-encapsulated metal nanoparticles: synthesis, characterization, and applications to catalysis, Acc. Chem. Res. 34 (3) (2001) 181–190.
[47] R. Wei, R. Zheng, C. Li, W. Wang, H. Zhang, Q. Sun, J. Lv, G. Zhang, L. Liu, X. Zhao, $ZrO_2$ superhydrophobic coating with an excellent corrosion resistance and stable degradation performance on Zr-based bulk metallic glass, Materials (Basel) 17 (1) (2023) 118.